WHAT CAN WE DO FOR SOFT X-RAY OPTICS BY RAY TRACING?

T. Namioka[1], T. Haga[2], and H. Kinoshita[3]

[1]Office of Naval Research Asian Office, 7-23-17 Roppongi, Minato-ku, Tokyo 106, Japan
[2]NTT System Electronics Laboratories, 3-1 Morinosato Wakamiya, Atsugi-shi 243-01, Japan
[3]Laboratory of Advanced Science and Technology for Industry, Himeji Institute of Technology, 2167 Shosha, Himeji-shi 671-22, Japan

1. Introduction

The advent of third-generation synchrotron radiation (SR) sources, the development of ultra large scale integrated (ULSI) circuits, and the expanding development of space observatories have created an increasing need for high quality, well characterized optical components and systems for use in the soft x-ray (SXR) region. For high-brightness "third generation" SR sources, beamline optics are required to withstand extreme power loads while providing precisely tailored radiation to experimental stations. The ever-increasing density of integrated circuit patterns is approaching fundamental limits of what can be accomplished with ultraviolet excimer lasers, and next-generation microelectronics will require the development of sophisticated and complex SXR optical systems. Next-generation SXR space observatories also will require utilization of complex aspheric optical elements in their telescopes and spectrometers to achieve large aperture combined with the highest possible spatial and spectral resolutions. It should also be noted that the need for new high precision SXR optics and optical systems has pressing applications in many other fields, ranging from biology to materials research.

Due to short operating wavelengths, SXR optics must meet very stringent metrological requirements not usual to conventional optical elements used at longer wavelengths. The current lack of sufficiently precise, yet practically convenient metrological technologies presents varying degrees of difficulty in judging the quality of SXR optical components and the accuracy of an assembled optical system. At this stage of the development of SXR optics, it is desirable for manufacturers as well as users to have a practical design method as well as a simulation method that can provide tolerance estimates for the fabrication of optical components needed to secure the highest possible performance of a planned SXR optical system.

To contribute towards the achievement of these ends, we have developed practical methods which incorporated analytic formulas and appropriate definitions into a ray tracing method based on Fermat's principle. They were found to be effective not only in designing a multi-element optical systems but also in estimating tolerances for fabrication and assembly errors of optics and maximizing the performance of resulted systems. The principles of the methods and some applications are given.

2. Fermat's Principle and Ray-Tracing Formulas

The theory of geometrical optics can be developed on the basis of a single hypothesis, known as Fermat's principle [1]. For a diffraction grating, the light path function F for a ray originating from a point A and diffracted at a point P (ξ,w,l) on the nth groove toward an image point B is defined by $F = AP + PB + nm\lambda$. Here, m is the spectral order and λ is the wavelength of the ray PB. Since the surface of the grating blank is expressed by $\xi = f(w,l)$, F is also a function of w and l. Application of Fermat's principle to the light path function yields $\delta F = (\partial F/\partial w)\delta w + (\partial F/\partial l)\delta l = 0$. Fermat's principle as applied to the diffraction grating is now stated as $(\partial F/\partial w) = 0$ and $(\partial F/\partial l) = 0$, and more explicitly as

$$\begin{aligned} \partial F/\partial w &= (L-L')(\partial\xi/\partial w) + (M-M') + m\lambda(\partial n/\partial w) = 0, \\ \partial F/\partial l &= (L-L')(\partial\xi/\partial l) + (N-N') + m\lambda(\partial n/\partial l) = 0, \end{aligned} \quad (1)$$

where (L,M,N) and (L',M',N') are the direction cosines of the incident ray AP and those of the diffracted ray PB of

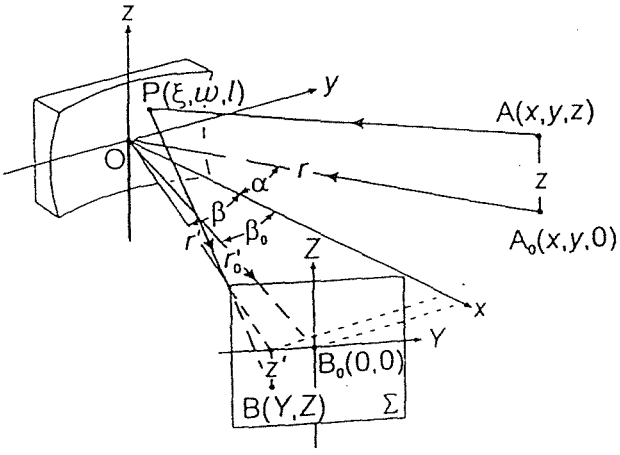

Fig. 1. Schematic diagram of the optical system.

Report Documentation Page

Form Approved
OMB No. 0704-0188

Public reporting burden for the collection of information is estimated to average 1 hour per response, including the time for reviewing instructions, searching existing data sources, gathering and maintaining the data needed, and completing and reviewing the collection of information. Send comments regarding this burden estimate or any other aspect of this collection of information, including suggestions for reducing this burden, to Washington Headquarters Services, Directorate for Information Operations and Reports, 1215 Jefferson Davis Highway, Suite 1204, Arlington VA 22202-4302. Respondents should be aware that notwithstanding any other provision of law, no person shall be subject to a penalty for failing to comply with a collection of information if it does not display a currently valid OMB control number.

1. REPORT DATE **1997**	2. REPORT TYPE	3. DATES COVERED **00-00-1997 to 00-00-1997**
4. TITLE AND SUBTITLE **What can we do for soft x-ray optics by ray tracing?**		5a. CONTRACT NUMBER
		5b. GRANT NUMBER
		5c. PROGRAM ELEMENT NUMBER
6. AUTHOR(S)		5d. PROJECT NUMBER
		5e. TASK NUMBER
		5f. WORK UNIT NUMBER
7. PERFORMING ORGANIZATION NAME(S) AND ADDRESS(ES) **Office of Naval Research Asian Office,7-23-7 Roppongi, Minato-ku, Tokyo, 106, Japan, , ,**		8. PERFORMING ORGANIZATION REPORT NUMBER
9. SPONSORING/MONITORING AGENCY NAME(S) AND ADDRESS(ES)		10. SPONSOR/MONITOR'S ACRONYM(S)
		11. SPONSOR/MONITOR'S REPORT NUMBER(S)
12. DISTRIBUTION/AVAILABILITY STATEMENT **Approved for public release; distribution unlimited**		
13. SUPPLEMENTARY NOTES		
14. ABSTRACT		
15. SUBJECT TERMS		

16. SECURITY CLASSIFICATION OF:			17. LIMITATION OF ABSTRACT	18. NUMBER OF PAGES	19a. NAME OF RESPONSIBLE PERSON
a. REPORT **unclassified**	b. ABSTRACT **unclassified**	c. THIS PAGE **unclassified**	**Public Release**	**14**	

Standard Form 298 (Rev. 8-98)
Prescribed by ANSI Std Z39-18

wavelength λ in mth order, respectively, and they are defined as

$$L = (\xi - x)/AP, \quad M = (w-y)/AP, \quad N = (l-z)/AP, \quad L' = (x'-\xi)/PB, \quad M' = (y'-w)/PB, \quad N' = (z'-l)/PB. \tag{2}$$

Solving these equations simultaneously, we obtain

$$L' = L + T, \qquad M' = M + m\lambda\frac{\partial n}{\partial w} - T\frac{\partial \xi}{\partial w}, \qquad N' = N + m\lambda\frac{\partial n}{\partial l} - T\frac{\partial \xi}{\partial l},$$

$$T = \frac{1}{e}\left[p + \sqrt{p^2 - eq}\right], \qquad e = 1 + \left(\frac{\partial \xi}{\partial w}\right)^2 + \left(\frac{\partial \xi}{\partial l}\right)^2, \tag{3}$$

$$p = -L + \left(M + m\lambda\frac{\partial n}{\partial w}\right)\frac{\partial \xi}{\partial w} + \left(N + m\lambda\frac{\partial n}{\partial l}\right)\frac{\partial \xi}{\partial l}, \qquad q = 2m\lambda\left(M\frac{\partial n}{\partial w} + N\frac{\partial n}{\partial l}\right) + (m\lambda)^2\left[\left(\frac{\partial n}{\partial w}\right)^2 + \left(\frac{\partial n}{\partial l}\right)^2\right].$$

All the equations derived above hold for gratings of any type, and the direction cosines (L', M', N') of the diffracted ray PB can be computed whenever the surface figure $\xi = f(w,l)$ and the groove pattern $n = h(w,l)$ are known.

We consider two image planes Σ and Σ_0, both of which are perpendicular to the x-y plane and pass through a point $B_0(x_0', y_0', 0)$ on the diffracted principal ray of wavelength λ in mth order, the incident principal ray being A_0O. The plane Σ_0 is perpendicular to the diffracted principal ray OB_0. The plane Σ makes an angle ϕ with the plane Σ_0:

$$x'\cos(\beta_0 + \phi) + y'\sin(\beta_0 + \phi) = r_0'\cos\phi. \tag{4}$$

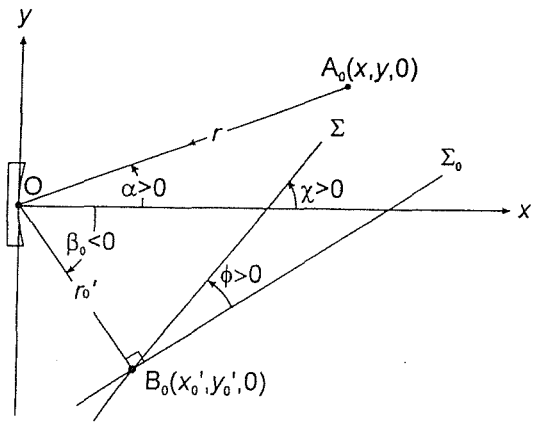

Fig. 2. Schematic diagram of two image planes Σ and Σ_0.

Here, β_0 is the angle of diffraction of the principal ray A_0OB_0, $\phi = 0$ for a monochromator, $\phi = \chi - \beta_0 - \pi/2$ for a flat-field spectrograph, and a series of image planes Σ with $\phi = \beta_0$ represents the focal plane for a Rowland-circle spectrograph. Thus, the intersection $B(x', y', z')$ of the ray PB with the image plane Σ, i.e., the coordinates of the ray-traced spot are determined:

$$x' = \xi + L'd, \qquad y' = w + M'd, \qquad z' = l + N'd,$$

$$d = [r_0'\cos\phi - \xi\cos(\beta_0+\phi) - w\sin(\beta_0+\phi)]/[L'\cos(\beta_0+\phi) - M'\sin(\beta_0+\phi)]. \tag{5}$$

For convenience we introduce in the plane Σ a new rectangular coordinate system whose Y axis lies in the x-y plane and Z axis is parallel to the z axis. The ray-traced image point $B(x', y', z')$ is then expressed in the new coordinates as $B(Y,Z)$:

$$Y = (y' - r_0'\sin\beta_0)\sec(\beta_0 + \phi), \qquad Z = z'. \tag{6}$$

3. Hybrid Design Method

It is desirable to have a practical method of designing a multiple-element optical system consisting of aspheric mirrors and varied-line-space and curved-groove gratings, both ruled and holographic. For this we have developed a hybrid design method which takes the advantages of both the ray-tracing and analytic methods [2].

The hybrid method optimizes design parameters by minimizing an analytic merit function $Q = \Sigma_i Q(\lambda_i)$ whose component $Q(\lambda_i)$ closely represents the variance of the spots formed when an infinite number of rays of a design wavelength λ_i are traced through the optical system concerned [3]. A component of the merit function is defined as

$$Q(\lambda_i) = q_Y^2(\lambda_i) + \mu q_Z^2(\lambda_i) = \frac{1}{WLH}\int_{-W/2}^{W/2}\int_{-L/2}^{L/2}\int_{-H/2}^{H/2}\left(Y - \bar{Y}\right)^2 dw\,dl\,dz + \frac{\mu}{WLH}\int_{-W/2}^{W/2}\int_{-L/2}^{L/2}\int_{-H/2}^{H/2} Z^2\,dw\,dl\,dz, \tag{7}$$

where λ_i is a wavelength chosen in the required scanning range, W and L are the width and height of the illuminated portion of the ruled area, respectively, H is the entrance slit height, and

$$\bar{Y} = \frac{1}{WLH}\int_{-W/2}^{W/2}\int_{-L/2}^{L/2}\int_{-H/2}^{H/2} Y \, dw\, dl\, dz ,$$

$$q_Y^2(\lambda_i) = \frac{1}{12}W^2 f_{100}^2 + \frac{1}{360}\left[W^4(2f_{200}^2 + 9f_{100}f_{300}) + 2L^4 f_{020}^2 + 2H^4 f_{002}^2\right] + \frac{1}{144}\left[2W^2 f_{100}(L^2 f_{120} + H^2 f_{102}) + L^2H^2 f_{011}^2\right]$$
$$+ \frac{1}{960}W^2\left[2W^2 f_{300}(L^2 f_{120} + H^2 f_{102}) + L^4 f_{120}^2 + H^4 f_{102}^2\right] + \frac{1}{448}W^6 f_{300}^2 + \frac{1}{1728}W^2L^2H^2(f_{111}^2 + 2f_{120}f_{102}), \quad (8)$$

$$q_Z^2(\lambda_i) = \frac{1}{12}\left(L^2 g_{010}^2 + H^2 g_{001}^2\right) + \frac{1}{144}\left\{W^2L^2(g_{110}^2 + 2g_{010}g_{210}) + H^2\left[W^2(g_{101}^2 + 2g_{001}g_{201}) + 2L^2(g_{010}g_{012} + g_{001}g_{021})\right]\right\}$$
$$+ \frac{1}{40}L^4 g_{010}g_{030} + \frac{1}{960}\left[W^2L^2 g_{210}(W^2 g_{210} + 2L^2 g_{030}) + L^2H^2 g_{012}(2L^2 g_{030} + H^2 g_{012}) + H^2(W^4 g_{201}^2 + L^4 g_{021}^2)\right]$$
$$+ \frac{1}{448}L^6 g_{030}^2 + \frac{1}{864}W^2L^2H^2(g_{210}g_{012} + g_{021}g_{201}).$$

In brief, for a given optical geometry, we (1) generate nine rays (n = 1,2,···,9) of wavelength λ_i randomly from the source, (2) determine the intersections of nth ray with the surfaces of the grating and the image plane, (w_n, l_n) and (Y_n, Z_n), by means of ray tracing, (3) substitute the values of (w_n, l_n), (Y_n, Z_n), and the height z_n of the source point into the analytic formulas for the spot diagrams

$$Y_n = w_n f_{100} + w_n^2 f_{200} + l_n^2 f_{020} + l_n z_n f_{011} + z_n^2 f_{002} + w_n^3 f_{300} + w_n l_n^2 f_{120} + w_n l_n z_n f_{111} + w_n z_n^2 f_{102} + \cdots,$$
$$Z_n = z_n g_{001} + l_n g_{010} + w_n l_n g_{110} + w_n z_n g_{101} + w_n^2 l_n g_{210} + w_n^2 z_n g_{201} + l_n^3 g_{030} + l_n^2 z_n g_{021} + l_n z_n^2 g_{012} + \cdots, \quad (9)$$

(4) solve the nine simultaneous equations for f_{ijk}'s and g_{ijk}'s, (5) repeat steps (1)-(4) for the other design wavelengths, and (6) calculate $Q(\lambda_i)$'s with the values of the f_{ijk}'s and g_{ijk}'s. Finally, the design parameters are determined by minimizing the merit function $Q = \Sigma_i Q(\lambda_i)$. If necessary, we may use $Q = \Sigma_i \epsilon(\lambda_i)Q(\lambda_i)$, $\epsilon(\lambda_i)$ being a weighting factor.

4. Resolving Power

4. 1. Spectroscopic Systems

The resolving power of spectroscopic systems, $\Re = \lambda/\Delta\lambda$, may be defined, in accordance with the Rayleigh criterion, by assuming that two similar spectrum lines of λ and $\lambda+\Delta\lambda$ are resolved when their contours cross at the point of each whose height is $4/\pi^2$ of the maximum (see Fig. 3a). In this case, $\Delta\lambda$ is the full width of the ray-traced line profile at its $(4/\pi^2)$-maximum point. The resolving power thus defined is denoted by $\Re(1)$. This definition would be appropriate only when spectral images have symmetric profiles of Gaussian type. To take into account the effect of asymmetric line profiles, we define the resolving power $\Re(2)$ by introducing an effective Gaussian line profile in place of an actual asymmetric line profile (refer to Fig. 3b for defining the effective Gaussian profile) [2].

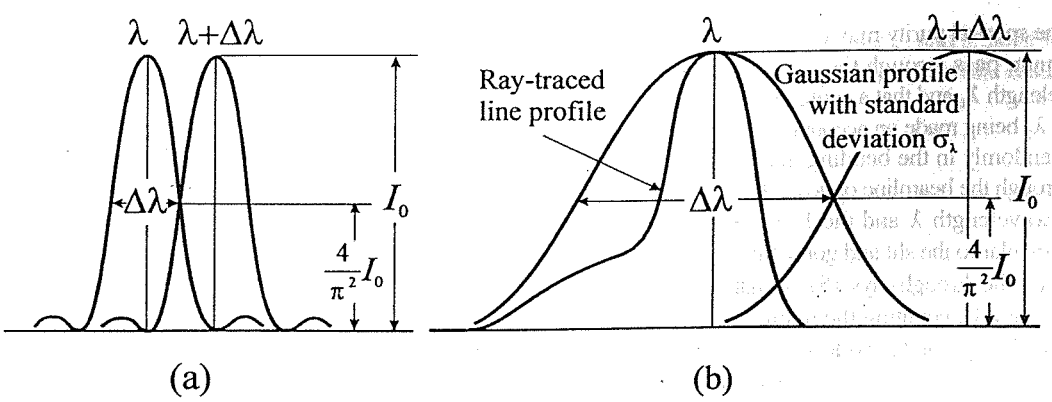

Fig. 3. Definitions of the resolving power based (a) on the Rayleigh criterion and (b) on the effective Gaussian profiles.

To define the resolving power $\Re(2)$, we (1) calculate the standard deviation σ_Y of ray-traced spots in the direction of dispersion, (2) convert σ_Y to the standard deviation σ_λ of the spectral spread for the rays of wavelength λ by multiplying the reciprocal linear dispersion at λ, (3) represent the line profile under consideration by an effective Gaussian profile whose standard deviation is given by σ_λ, and (4) assume that two similar spectral lines of λ and $\lambda+\Delta\lambda$ are resolved when their effective Gaussian lines are separated by $\Delta\lambda=2.643\sigma_\lambda$ to make the minimum resultant intensity between the lines $8/\pi^2$ as great as the resultant intensity at the central maximum of either of the lines. Thus the resolving power $\Re(2)$ is defined by

$$\Re(2) = \lambda/\Delta\lambda = \lambda/2.643\,\sigma_\lambda. \tag{10}$$

4. 2. Demagnifying Projection Lithography Systems

The square-wave modulation transfer function (MTF) has frequently been used to evaluate the imaging characteristics of demagnifying projection optics [4]. On referring to our previous experience gained through projection lithographic processes including resist processes, we assume that a projected line-and-space pattern at a given spatial frequency is properly resolved when the modulation of the intensity distribution of the mask image formed on a wafer is 45% or more.

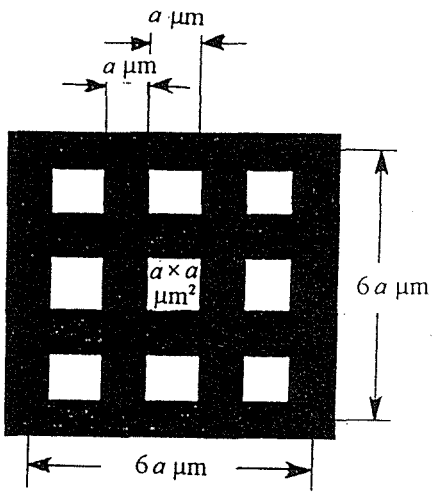

Fig. 4. Source pattern on the mask.

To estimate the performance of a demagnifying projection optics by means of ray tracing, we (1) consider a grid pattern of a-μm line-and-space on the reflection mask (see Fig. 4), (2) assume that the space portion of this grid pattern emits light into the entrance pupil of the system, (3) choose three $6a \times 6a$-μm^2 areas centered around the two corner points at the right (or left) and the central point of the ring field formed on the mask, and take these areas as distributed light sources, each containing 9 elemental sources of $a \times a$ μm^2, (4) generate rays randomly from each one of these three areas and construct spot diagrams in the plane of the wafer by tracing rays through the projection optics, (5) construct the intensity distributions of the projected image in the two directions, x and y, parallel to the grid lines by counting the number of spots falling into individual zones of $(6aM/100)$-μm wide taken in the x and y directions, M being the magnification of the projection optics, and (6) estimate the modulation of the intensity profiles of the pattern thus obtained in the two directions and apply the "≥45%" criterion to the estimated modulations.

5. Spectral Purity

The spectral purity of the beam emerging from the exit slit is an important factor in evaluating the performance of a high-resolution monochromator on a synchrotron radiation beamline, whose source is of continuum. It is also important that the resolving power estimated should not contradict with the spectral purity.

The spectral purity may be examined by analyzing the frequencies at which rays of various wavelength components of the continuum pass through the exit slit of a given width. Referring to Fig. 5, we (1) assume that the monochromator is tuned to a wavelength λ_0 and that a continuum band which extends over a range of $\lambda_1 \le \lambda \le \lambda_2$ is incident on the grating, choice of the limits λ_1 and λ_2 being made on account of the reciprocal linear dispersion, (2) generate rays of various wavelengths in the continuum band randomly in the bending magnet source or the central cone of the undulator under consideration and trace the generated rays through the beamline optics until the number of rays passed through the exit slit reaches 1000, (3) identify each through-ray by its wavelength λ and the Y coordinate of its intersection with the plane of the exit slit, the Y axis being taken as the line perpendicular to the slit and going through the center of the slit opening, (4) construct the spectral purity plot diagram by plotting (λ,Y)'s for the through-rays, (5) estimate from the spectral purity plot diagram the frequency distribution $\nu(\lambda)$ of the wavelength component λ by counting the number of points (λ,Y)'s falling onto individual parallel zones having a width of $(\lambda_2-\lambda_1)/100$ nm and a height equal to the width of the exit slit, and (6) calculate the spectral purity A_R/A_T, where A_R and A_T are the area under the frequency distribution curve between $(\lambda_0-1.3215\sigma_\lambda)$ nm and $(\lambda_0+1.3215\sigma_\lambda)$ nm and the total area under the whole curve, respectively.

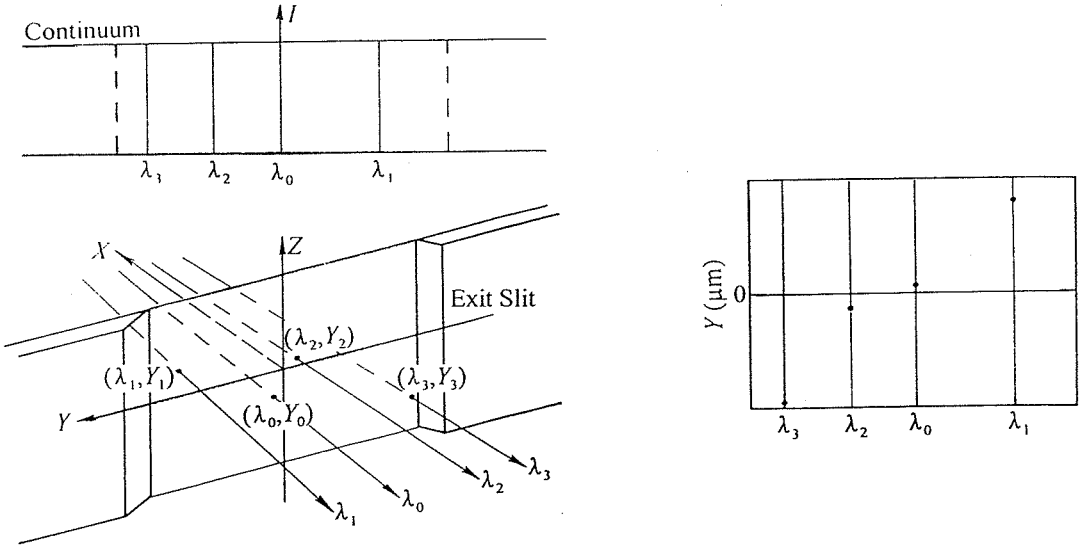

Fig. 5. Intensity distribution of the continuum band and explanations of through-rays and spectral purity plot diagrams.

6. Slope error and figure error

We consider an ellipsoidal mirror whose surface figure is defined by

$$\xi = A - A\sqrt{1 - \left(\frac{w^2}{B^2} + \frac{l^2}{C^2}\right)} + \Delta\xi \tag{11}$$

in a rectangular coordinate system attached to the mirror. The vertex O of the mirror is taken as the coordinate origin and the mirror normal at O as the x axis. In Eq. (11), A, B, and C are the ellipsoidal semiaxes with respect to the x, y, and z axes, respectively, and (ξ,w,l) are the coordinates of a point P on the mirror surface. The quantity $\Delta\xi$ is the deviation from the ideal ellipsoidal surface, and is assumed to be constituted of the surface figure error $\Delta\xi_{FE}$ and thermal deformation $\Delta\xi_{TD}$:

$$\Delta\xi = \Delta\xi_{FE} + \Delta\xi_{TD}. \tag{12}$$

The figure error arises from the imperfection in polishing the surface of a mirror or a grating blank, and it often is represented by values of the slope error. We assume that the slope errors s_y and s_z at $P(\xi,w,l)$ in the y and z directions are distributed randomly with a probability density function

$$f(s_y,s_z) = \frac{1}{2\pi\sigma_1\sigma_2}\exp\left[-\frac{1}{2}\left(\frac{s_y^2}{\sigma_1^2} + \frac{s_z^2}{\sigma_2^2}\right)\right], \tag{13}$$

where σ_1 and σ_2 are the standard deviations of s_y and s_z, respectively. We assumed here that the s_y and s_z have no mutual correlation and their respective averages over the mirror surface are zero. The sequence, $\{(s_y, s_z)_i\}$, of normal random slope errors with the probability density $f(s_y,s_z)$ are generated from

$$\begin{aligned}(s_y)_i &\equiv \left[\partial(\Delta\xi_{FE})/\partial w\right]_i = \sigma_1(-2\log_e u_i)^{1/2}\cos 2\pi u_{i+1},\\ (s_z)_i &\equiv \left[\partial(\Delta\xi_{FE})/\partial l\right]_i = \sigma_2(-2\log_e u_i)^{1/2}\sin 2\pi u_{i+1},\end{aligned} \tag{14}$$

with the aid of the sequence $\{u_i\}$ of uniform random numbers on the interval [0,1].

The corresponding figure error $\Delta\xi_{FE}$ is obtained by integrating $d(\Delta\xi_{FE}) \equiv s_x dw + s_y dl$ under an assumption $\sigma_1 = \sigma_2 \equiv \sigma_{SE}$:

$$\Delta \xi_{FE} = \sigma_{SE}(-2\log_e u_i)^{1/2}(w\cos 2\pi u_{i+1} + l\sin 2\pi u_{i+1}). \tag{15}$$

7. SR Beamline Optics

Examples are given for the design, resolving power, spectral purity of an undulator beamline optics, and thermal deformation.

7. 1. Validity of various ray-deviation formulas

Equations (9) express the aberrations (up to third order) in spectral images formed in the plane Σ (see Fig.2). They represent ray-traced spot diagrams also, and they are called spot diagram (SD) formulas. The accuracy of Eqs. (9) is limited only by the neglect of the fifth- and higher-order terms in performing power series expansions.

It is of practical interest to examine, with reference to exact ray tracing, the validity of the SD formulas and also that of similar formulas based on light path function (LPF). The LPF-based formulas, which are widely in use for the design of grating instruments, are given by [5]

$$Y = r_0'\sec\beta_0(\partial F/\partial w), \qquad Z = -(zr_0'/r) + r_0'(\partial F/\partial l), \tag{16}$$

where the image plane is assumed to be perpendicular to the principal diffracted ray (Σ_0 in Fig. 2 and $\phi = 0$ in Eq. (4)). The expansion coefficients of the light path function F contain the coordinates (r',β,z') of point B, which are unknown functions of the coordinates (ξ,w,l) of point P (see Fig. 1). Partial differentiation of F therefore is not possible in principle. To circumvent this problem, it is customarily assumed that the deviation of the spot B formed by the ray APB from the spot B_0 of the principal ray AOB_0 in the image plane is negligible so that the unknown quantities r', β, and z' in the expansion coefficients of the light path function can be approximated by the corresponding quantities r_0', β_0, $-zr_0'/r$, which are all associated with the principal ray A_0OB_0:

$$F \approx [F]_{r'=r_0',\,\beta=\beta_0,\,z'=-zr_0'/r}. \tag{17}$$

With this approximation, Eqs. (16) are expressed as

$$Y = r_0'\sec\beta_0\left[wF_{200} + \frac{3}{2}w^2F_{300} + \frac{1}{2}l^2F_{120} + lzF_{111} + \frac{1}{2}z^2F_{102} + O\left(\frac{w^3}{R^3}\right)\right], \tag{18}$$

$$Z = r_0'\left[-\frac{z}{r} + lF_{020} + wlF_{120} + wzF_{111} + O\left(\frac{w^3}{R^3}\right)\right]. \tag{19}$$

It can be shown analytically that the LPF-based formulas are correct to third order only when $\beta_0 = 0$ and the tangential and sagittal focal curves cross on the grating normal [1]. The same results are obtained [1] for another ray-deviation formulas that are based on the wavefront aberration (WFA) theory [6,7]. In practice these LPF- and WFA-based formulas can safely be applied to cases in which defocus (F_{200}) and astigmatism (F_{020}) are small over the design wavelength range (i.e.,the corresponding angles of diffraction β_0 are not too large).

The validity of individual formulas is depicted clearly in Fig. 6, which compares the spot diagrams generated for a 142° constant-deviation grazing incidence monochromator by the SD- and LPF-based formulas with those constructed by exact ray tracing. Specifications of the monochromator are: wavelength range, 15 nm - 150 nm; $m = +1$; $r = 319.9$ mm; $r_0' = 317.8$ nm; $R = 1000$ mm; $1/\sigma = 550$ grooves/mm; $2a = 3.877791 \times 10^{-9}$ mm; $6b = -6.844844 \times 10^{-14}$ mm; $4c = 3.654780 \times 10^{-20}$ mm; and ruled area, 60 (W) × 30 (L) mm^2. The monochromator has a rather large astigmatism as can be seen in Fig. 6. The spot diagrams in Figs. 6b (SD-based formulas) are very similar to the corresponding ones in Fig. 6a (ray tracing), proving the validity of the SD-based formulas. On the other hand, the spot diagrams generated from the LPF-based formulas (Fig. 6c) are quite different in shape and magnitude from those constructed by exact ray tracing and the SD-based formulas. Spot diagrams constructed by the WFA-based formulas also deviate considerably from Figs. 6a and 6b (see Ref. 1). These results show the

limitation in the applicability of the LPF- and WFA-based formulas to a system in which astigmatism is not corrected to a sufficient degree.

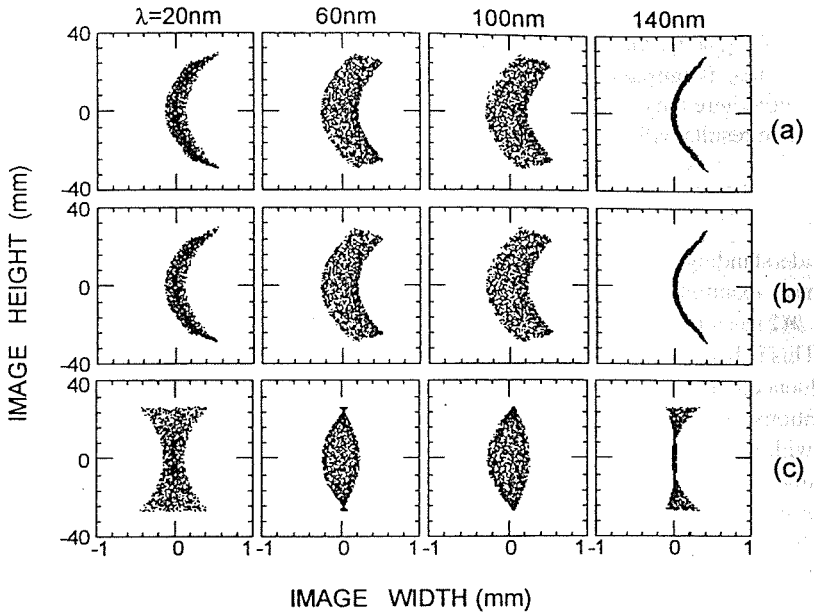

Fig. 6. Spot diagrams constructed for the 142° constant-deviation grazing incidence monochromator with (a) exact ray tracing, (b) SD formulas, and (c) LPF formulas.

7. 2. Design, resolving power, and spectral purity of undulator beamline optics

A. Design

We consider an objective Monk-Gillieson (M-G) type grazing incidence VLS plane grating monochromator (PGM) shown in Fig. 7. A fixed spherical concave mirror M accepts radiation from a source point S at an angle of incidence 88° and delivers a converging beam onto a ruled VLS plane grating G at an angle of incidence α. The diffracted rays of wavelength λ in mth order are focused onto the fixed exit slit Ex after reflected by a movable plane mirror M'. Wavelength scanning is carried out by combining simultaneous translation and rotation of M' with simple rotation of G so that the direction of the exiting beam remains unchanged.

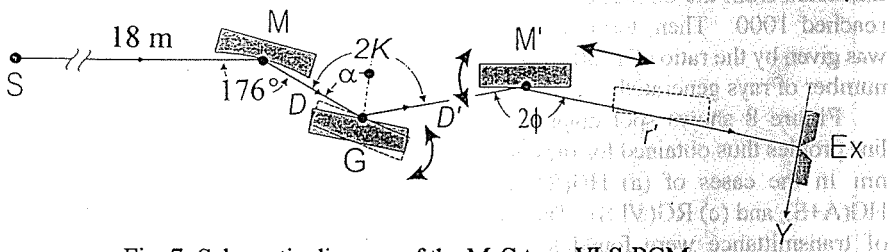

Fig. 7. Schematic diagram of the M-G type VLS-PGM

This monochromator, M-G type VLS PGM, was designed by means of the hybrid method described in Section 3. The design conditions and the results are summarized below.

Given conditions: $r \equiv$ SM = 18000 mm, $\theta = 88°$, R (radius of curvature of M) = 155700 mm, $D \equiv$ MG = 200 mm, $\phi - K = 1°$, σ = 1/2400 mm, ruled area = 60 (W) × 25 (L) mm^2, spectral order $m = +1$, and wavelength range = 0.5 - 10 nm.
Designed parameters: $2a = 1.762906\times10^{-10}$ mm, $6b = 5.299280\times10^{-17}$ mm, $4c = 1.354672\times10^{-23}$ mm, $D' \equiv$ GM' = 401.10 mm at λ=5 nm, and $r' \equiv$ M'Ex = 1647.78 mm at λ=5 nm. (Note here that D' and r' are wavelength dependent.)

We also designed holographic plane gratings for the monochromator under the same given conditions as described above for the ruled VLS gratings. We designate the holographic gratings (HG) recorded with (1) two spherical wave fronts and (2) an aspheric and a spherical wave front as HG(S+S) and HG(A+S), respectively, and the ruled VLS gratings as RG(VLS). The design parameters thus obtained with λ_0=441.6 nm are summarized below.

HG(S+S): $r_C = -2194.42$ mm, $\gamma = -71.2090°$; $r_D = 959.60$ mm, $\delta = 6.4964°$.
HG(A+S): $R_1 = 1200$ mm, $p_C = 585.44$ mm, $q_C = 614.96$ mm, $\eta_C = -35.3665°$, $\gamma = -36.8560°$; $r_D = 979.50$ mm, $\delta = 27.3893°$.

The performance of all the gratings thus designed was evaluated in terms of resolving power and spectral purity determined from ray-traced spot diagrams, assuming L_u (undulator length) = 4.4 m, $\sigma_y = 41.1$ μm, $\sigma_z = 212.7$ μm, $\sigma_y' = 9.7$ μrad, and $\sigma_z' = 18.9$ μrad.. We considered here the effect of aberrations only and put aside any contribution from higher order overlapping and surface scattering. The results will be given in the following subsections B and C.

B. Resolving power

To gain a better understanding of the resolving power, we have examined the behavior of $\mathcal{R}(1)$ and $\mathcal{R}(2)$ as a function of the ruled width W. This is because the resolving power is influenced directly by the amount of aberrations in spectral images, which increase with increasing W. We constructed spot diagrams and line profiles for the three gratings HG(S+S), HG(A+S), and RG(VLS) as a function of W. The ruled width was varied by masking down the ruled area stepwise from W=60 mm (full ruled width) to W=7.5 mm by a factor of 0.5, while keeping the groove length unmasked (L=30 mm). To take into account these four different masked apertures on the grating, we also computed the transmittance of rays through the respective apertures. For this, rays were generated randomly in the central cone of the undulator until the number of rays diffracted from the unmasked ruled-area reached 1000. Then, the transmittance was given by the ratio of 1000 to the total number of rays generated.

Figure 8 shows spot diagrams and line profiles thus obtained for rays of λ=5 nm in the cases of (a) HG(S+S), (b) HG(A+S), and (c) RG(VLS). The values of transmittance were found to be the same in all the cases (a), (b), and (c); 28.83%, 55.25%, 88.42%, and 99.80% for W =7.5, 15, 30, and 60 mm, respectively. These values were taken into consideration in drawing the line profiles. The full width, ΔW_F, of the individual line profiles at their $(4/\pi^2)$-maximum points is indicated by arrows and the effective Gaussian line profiles are shown by dotted lines. Before examining the behavior of $\mathcal{R}(1)$ and $\mathcal{R}(2)$, we should estimate their statistical dispersion arising from random generation of rays. For this we constructed spot diagrams and line profiles by tracing 1000 diffracted rays for ten different sets of randomly generated rays of 5 nm through the individual gratings of Fig. 8 as a function of the width W of the unmasked portion of the ruled area. The resulted spot diagrams and line profiles were found to be very similar to the corresponding ones in Fig. 8. The mean values of $\mathcal{R}(1)$ and $\mathcal{R}(2)$ obtained are summarized in Table I. The statistical dispersion of $\mathcal{R}(1)$ is much larger than that of $\mathcal{R}(2)$, but not large enough to alter any conclusion to be drawn from their mean values.

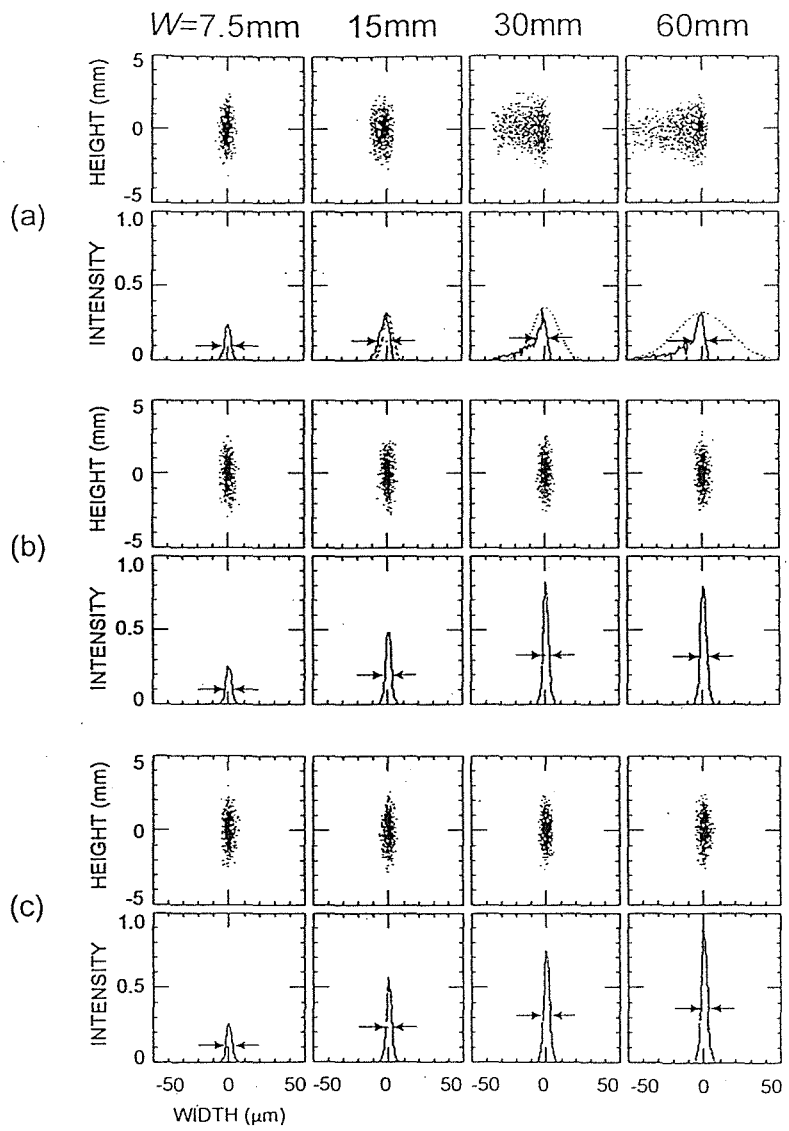

Fig. 8. Spot diagrams and line profiles constructed as a function of the ruled width W for the M-G type VLS-PGM equipped with (a) HG(S+S), (b) HG(A+S) or (c) RG(VLS).

For HG(S+S) we notice in Table I that with an increase in W, the gradual decrease in $\mathfrak{R}(1)$ forms a sharp contrast to the rapid decrease in $\mathfrak{R}(2)$. We also note in Fig. 8a (1) that the line profile rapidly develops shading (coma-type aberrations) with increasing W, while Δw_F remains nearly unchanged and (2) that the effective Gaussian line profile nearly coincides with the ray-traced line profile for $W = 7.5$ and 15 mm, whereas those for $W = 30$ and 60 mm are much wider than the corresponding ray-traced line profiles.

Table I. Mean values of the resolving powers $\mathfrak{R}(1)$ and $\mathfrak{R}(2)$ of the M-G type VLS-PGM as a function of the width W of the unmasked portion of the ruled area.

W (mm)	HG (S+S)		HG(A+S)		RG(VLS)	
	$\mathfrak{R}(1)$	$\mathfrak{R}(2)$	$\mathfrak{R}(1)$	$\mathfrak{R}(2)$	$\mathfrak{R}(1)$	$\mathfrak{R}(2)$
7.5	28100	28300	29200	29800	28600	29900
15	18500	18600	28500	29600	29300	29600
30	16100	6400	28000	29200	28100	29600
60	14300	2900	27800	28500	28000	29200

HG(A+S) and RG(VLS) exhibit a striking contrast to HG(S+S) in their behavior with changes in W. Regardless of the width W of the unmasked portion of the ruled area, both HG(A+S) and RG(VLS) provide nearly the same value of ~29000 for $\mathfrak{R}(1)$ and $\mathfrak{R}(2)$ and also maintain sharp Gaussian type line profiles. These findings suggest the need for careful examination of the resolving power in relation with the spectral purity of the beam emerging from the exit slit.

C. Spectral purity

The spectral purity of the beam emerging from the exit slit of the M-G type VLS-PGM was examined by analyzing the frequencies at which rays of various wavelength components passed through the exit slit of 5-μm wide. For this, we assumed that the monochromator was tuned to a wavelength of 5 nm and that a continuum band which extends over a range of 4.995 nm ≤ λ ≤ 5.005 nm was incident on the grating. Rays of various wavelengths in the continuum band were generated randomly in the central cone of the undulator and were traced through the monochromator equipped with HG(S+S), HG(A+S) or RG(VLS) until the number of rays passed through the exit slit reached 1000. Each through ray is identified by its wavelength λ and the Y coordinate (see Fig. 7) of its intersection with the plane of the exit slit. Plotting (λ, Y)'s for the through rays, we obtain a diagram similar to the spot diagram, which we call the spectral purity plot diagram. The frequency distribution $\nu(\lambda)$ of wavelength components of the continuum band is estimated for the through rays by counting the number of points (λ, Y)'s falling onto individual parallel zones of 5×10^{-5} nm wide and 5-μm high in the spectral purity plot diagram. The procedure of constructing the spectral purity profile is similar to that of making the line profile from the spot diagram.

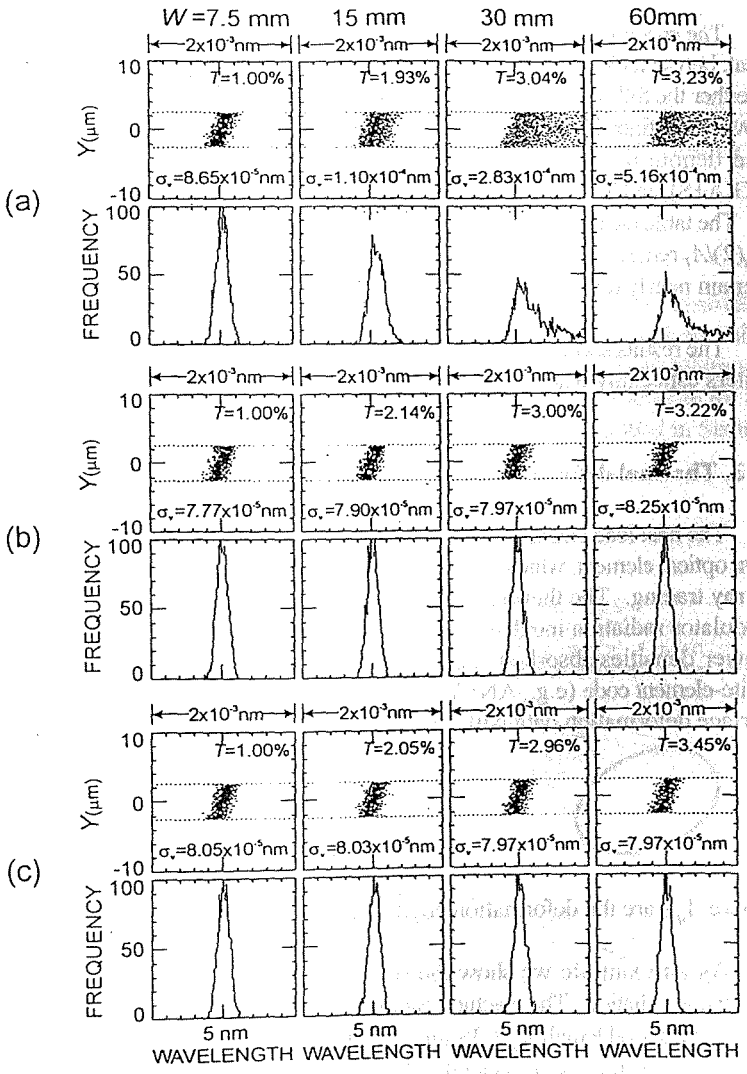

Fig. 9. Spectral purity plot diagram and spectral purity profiles constructed for the M-G type VLS-PGM as a function of the width W of the unmasked portion of the ruled area.

Figures 9a, 9b, and 9c show the

spectral purity plot diagrams and the corresponding spectral purity profiles obtained for W = 7.5, 15, 30, and 60 mm in the cases of HG(S+S), HG(A+S), and RG(VLS), respectively. The two horizontal dotted lines in each spectral purity plot diagram indicate a slit opening of 5 μm. The percentage T of all the rays generated that were through-rays is indicated at the top of the respective spectral purity plot diagrams. The standard deviation σ_ν of the distribution $\nu(\lambda)$ is given at the bottom of each diagram. The values of σ_ν are a measure of the spectral purity. In Fig. 9, it is interesting to note the following facts. When σ_ν is greater than 1.7×10^{-4} nm, the wavelength band-pass width corresponding to a slit opening of 5-μm, the spectral purity is degraded and the values of $\mathcal{R}(1)$ and $\mathcal{R}(2)$ are greatly different. In case (a) with W = 30 and 60 mm, σ_ν's are larger than 1.7×10^{-4} nm, and $\mathcal{R}(1) \approx 16100$ (or 14300) and $\mathcal{R}(2) \approx 6400$ (or 2900) for W = 30 mm (or 60 mm), respectively. In all other cases, $\sigma_\nu < 1.7\times10^{-4}$ nm, and $\mathcal{R}(1) \approx \mathcal{R}(2)$ regardless of the values of W.

Table II. Degree of the spectral purity of the beam emerging from the M-G type VLS-PGM as a function of the width W of the unmasked portion of the ruled area..

W (mm)	HG(S+S)		HG(A+S)		RG(VLS)	
	$A_{\mathcal{R}}(1)/A_T$	$A_{\mathcal{R}}(2)/A_T$	$A_{\mathcal{R}}(1)/A_T$	$A_{\mathcal{R}}(2)/A_T$	$A_{\mathcal{R}}(1)/A_T$	$A_{\mathcal{R}}(2)/A_T$
7.5	84 %	84 %	85 %	85 %	86 %	85 %
15	73	76	86	85	85	84
30	58	74	85	84	86	85
60	49	79	84	85	82	85

The spectral purity of the beam emerging from the exit slit may also be estimated from the ratio of the area $A_{\mathcal{R}}$ under the main peak between $(5 - \Delta\lambda/2)$ nm and $(5 + \Delta\lambda/2)$ nm and the total area A_T under the whole frequency distribution curve, where $\Delta\lambda$ is either the full width of the ray-traced line profile at its $(4/\pi^2)$-maximum point or $2.6423\sigma_\lambda$ according to whether the resolving power is defined by $\mathcal{R}(1)$ or $\mathcal{R}(2)$. Accordingly, we differentiate the area $A_{\mathcal{R}}$ specified by $\mathcal{R}(1)$ from the one designated by $\mathcal{R}(2)$ and denote the former by $A_{\mathcal{R}}(1)$ and the latter by $A_{\mathcal{R}}(2)$. The ratios $A_{\mathcal{R}}(1)/A_T$ and $A_{\mathcal{R}}(2)/A_T$ were computed for HG(S+S), HG(A+S), and RG(VLS) as a function of W, the width of the unmasked portion of the ruled area. The results are listed in Table II. The table clearly shows (1) that in the case of HG(S+S) the ratio $A_{\mathcal{R}}(1)/A_T$ rapidly decreases with an increase in W, whereas $A_{\mathcal{R}}(2)/A_T$ remains at ~80% regardless of W and (2) that in the cases of HG(A+S) and RG(VLS) all the ratios listed in the table remain nearly unchanged as W is varied and $A_{\mathcal{R}}(1)/A_T$ and $A_{\mathcal{R}}(2)/A_T$ are practically the same for all values of W.

The results shown in Figs. 8 and 9 and Tables I and II indicate that the definition of $\mathcal{R}(2)$ is more realistic as compared with others especially when the monochromator under consideration yields spectral images with asymmetric profiles.

7. 3. Thermal deformation

The heat load exerted on beamline optics by undulator radiation can distort their surfaces. The effect is the greatest on the first optical element, which is usually a mirror. The performance of such a thermally deformed mirror can be simulated by means of ray tracing. The thermal deformation is calculated in four steps: (1) calculation of individual harmonic power densities of undulator radiation incident on the mirror surface by means of a code such as URGENT [8], (2) calculation of the harmonic power densities absorbed at each mesh element on the mirror surface, (3) calculation of thermal deformation by means of a finite-element code (e.g., ANSYS, a commercial soft ware), and (4) derivation of an analytic expression of $\Delta\xi_{TD}$ by fitting the surface deformation data with a polynomial of the form

$$\Delta\xi_{TD} = \sum_{i,j} A_{ij} w^i l^j, \qquad 0 \le i + j \le 6, \tag{20}$$

where A_{ij}'s are the deformation coefficients.

As an example we show the result of a simulation made on the thermal deformation of a spherical mirror exposed to undulator radiation. The machine parameters assumed for the undulator are: wavelength of the fundamental radiation = 4.5 nm; undulator period length λ_u = 39 mm; number of magnet period N = 123; deflection parameter K =1.4057; electron energy / $m_e c^2$ (m_e, electron mass; c, velocity of light) = γ = 2395.08; rms transverse size of the electron beam in the horizontal direction σ_y = 0.330 mm; rms transverse size of the electron beam in the vertical direction σ_z = 0.063 mm; rms angular divergence of the electron beam in the horizontal direction σ_y' = 30 μrad; rms angular divergence of the electron beam in the vertical direction σ_z' = 16 μrad. The mirror is assumed to accept undulator radiation of 0.5 mrad (h) × 0.5 mrad (v) through a beam defining

aperture. It is also assumed that the mirror is a directly water-cooled metallic spherical concave mirror having the following specifications: radius of curvature R = 75 m; dimensions = 178 mm (W) × 66 mm (H) × 28 mm (D); blank material = brazed assembly of Glidcop™ and OFHC copper, whose surface is plated with electroless nickel; and water-cooling channel = machined series circuit with a rectangular cross section (hydraulic diameter = 0.4763 cm) for turbulent water flow (flow rate = 5.53 liters/min and Reynolds number > 4000).

The surface deformation of the mirror M is calculated by using URGENT and ANSYS. URGENT calculation shows that the mirror receives a total power of 209 W and absorbs 127 W on its surface. The results of ANSYS calculation are curve fitted to Eq. (20). This yields the thermally deformed surface of the spherical mirror M as

$$\begin{aligned}\xi = R - R[1 - (w^2 + l^2)/R^2]^{1/2} &+ 3.09499 \times 10^{-4} - 3.39872 \times 10^{-8} w^2 - 8.21102 \times 10^{-8} l^2 \\ &+ 4.75112 \times 10^{-12} w^4 + 4.833510 \times 10^{-11} w^2 l^2 - 4.880480 \times 10^{-7} l^4 - 3.812470 \times 10^{-16} w^6 \\ &- 1.569350 \times 10^{-14} w^4 l^2 + 5.484390 \times 10^{-12} w^2 l^4 + 2.030340 \times 10^{-8} l^6,\end{aligned} \tag{21}$$

where R is the radius of curvature of the mirror.

To evaluate the performance of this deformed mirror by means of ray-traced spot diagrams, it is required to incorporate Eqs. (15) and (21) into an exact ray tracing procedure. The ray-tracing procedure can easily be modified to meet the requirement by following the method given in Ref. 9. Rays from the central cone of the undulator can be generated by a simulation code [10] that takes into account the machine parameters and emission probability.

8. Demagnifying Projection Optics

Examples are given for the tolerance for the figure errors in the individual components of projection optics, the effect of figure errors in projection optics on the resolution of mask pattern images, and simulation of Foucault knife edge testing for assembly errors [11].

8. 1. Tolerance for the figure errors of ellipsoidal mirrors

A measure of figure errors that are allowable to achieve near diffraction limited performance of a mirror system is provided by Rayleigh's quarter wavelength rule [12] and the Maréchal condition [13]. These tolerance criteria give $\lambda/8$ peak-to-valley (P-V) and $\lambda/28$ rms for each mirror of the two-mirror system: 1.6 nm P-V and 0.46 nm rms for λ = 13 nm. These tolerances often are too tight in practice. It is therefore desirable to develop a means of obtaining a practically reasonable tolerance for the figure error. One approach to this task would be the use of ray tracing. We have tried to utilize the method described in Section 6 for exploring the possibility. For this we used the NTT's projection optics as an example.

The optical configuration of the NTT's EUV projection lithography system is illustrated in Fig. 10. The system consists of the illumination optics for producing a ring field on a reflection mask and the projection optics for imaging a reduced pattern of the mask on a wafer.

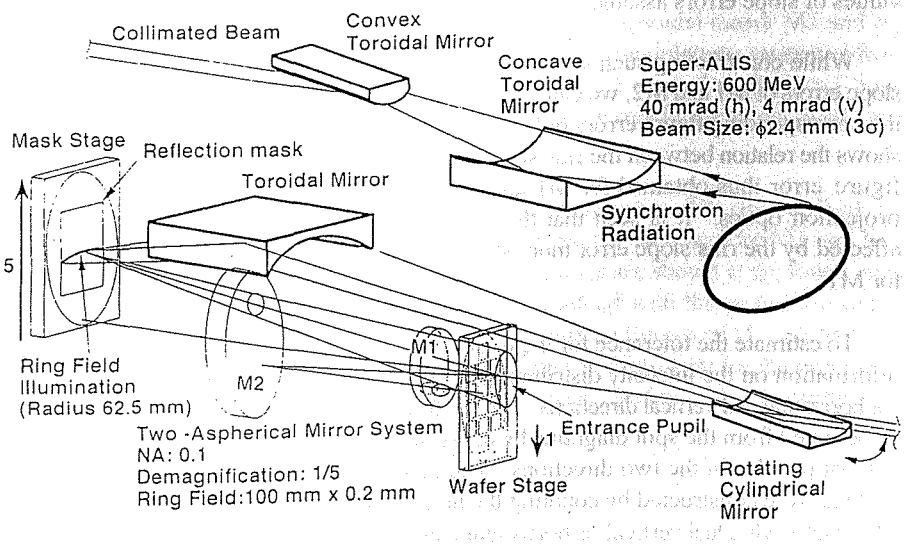

Fig. 10. Optical configuration of the NTT's EUV projection lithography system.

Synchrotron radiation of 40 mrad (h) × 4 mrad (v) from a 600 Mev, 500 mA (1.2 A max) superconducting compact electron storage ring at the NTT SR facility is shaped to a parallel beam of 20 mm (h) × 10 mm (v) by a concave toroidal mirror and a convex toroidal mirror and then focused on the reflection mask, RMK, by a rotatable concave cylindrical mirror and a concave toroidal mirror. The focused beam illuminates a ring field of 5 mm (h) × 1 mm (v) on RMK, the radius

of the ring image being 62.5 mm. The ring field is expanded to 100 mm (h) × 1 mm (v) by oscillating the cylindrical mirror through angles of ±53.13°, and it is further extended to 100 mm (h) × 125 mm (v) by translating RMK vertically.

The illuminated area of RMK is projected on the wafer by a demagnifying optics with a numerical aperture of 0.1 and a magnification of 1/5. The demagnifying optics is of telecentric and consists of a convex ellipsoidal mirror M1 of $k = \sim 10$ and a concave ellipsoidal mirror M2 of $k = \sim 0.1$, k being the conic coefficient (see Fig. 10). This coaxially symmetric two-mirror system was chosen because of its simplicity, reasonable aberration balancing, high throughput, relatively large fabrication tolerance, and easy assembling. The diameters of M1 and M2 are 60 mm and 150 mm, respectively, and both the mirrors have almost the same radius of curvature, ~500 mm. The surfaces of M1 and M2 are very close to sphere: the maximum deviation of the surface figure of M1 (or M2) from its reference spherical surface is less than 0.6 (or 2.0) μm. An addition of vertical translation of the wafer to the motions of the rotatable cylindrical mirror and RMK will produce the image of 20 mm (h) × 25 mm (v) on the wafer.

To estimate a practically reasonable tolerance for the figure error of the demagnifying projection optics, we follow the procedures described in Sections 4.2 and 6. We consider a 0.5-μm line-and-space grid pattern on the reflection mask and assume that the space portions of this grid pattern emit light into the entrance pupil of the system. We choose three 3 × 3 μm² areas, A, B, and C. The areas A and B are taken at around the two corner points at the right (or left) of the ring field of 5 mm (h) × 1 mm (v) formed on RMK and the area C is taken at around the center of the ring field. We consider these area as distributed light sources , each containing 9 elemental sources of 0.5 μm × 0.5 μm. Ten thousand rays generated from each one of these three sources A, B, and C were traced through the convex ellipsoidal mirror M1 and the concave ellipsoidal mirror M2. The spot diagrams thus obtained with the three sources were found to be indistinguishable from one another as far as the same slope errors are assumed for the projection system. In Fig. 11 are shown, as an example, the spot diagrams constructed for the source C and for certain values of slope errors assumed on M1 and M2.

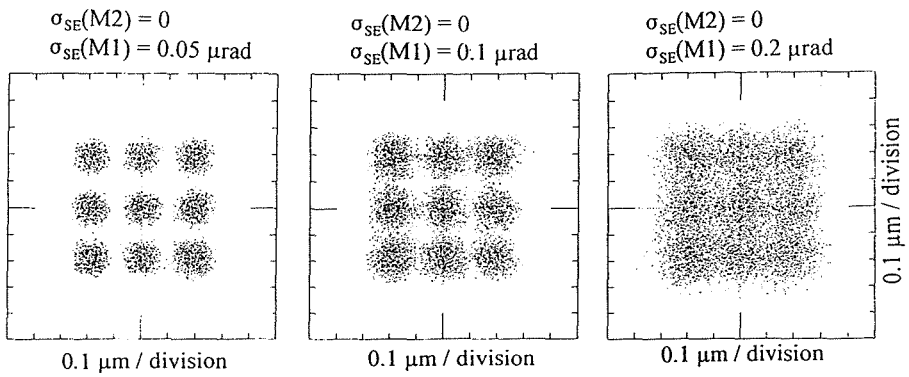

Fig. 11. Ray-traced images of the source pattern C on the mask. The source pattern is of Fig. 4 with $a = 0.5$ μm. σ_{SE} is the rms slope error of the mirror specified in parentheses. M1 and M2 are the convex and the concave ellipsoidal mirror.

While constructing such spot diagrams with assumed slope errors of M1 and M2, we can calculate from Eq. (15) the corresponding figure errors of M1 and M2. Figure 12 shows the relation between the rms slope error and the rms figure error thus obtained for M1 and M2 of the NTT's projection optics. It is seen that the rms figure error is affected by the rms slope error more strongly for M2 than for M1.

To estimate the tolerance for the figure error, we need information on the intensity distributions of the images in the horizontal and vertical directions. Such information can be obtained from the spot diagrams by constructing image pattern profiles in the two directions. The image pattern profiles were constructed by counting the number of spots falling into individual vertical or horizontal zones of 0.006-μm in width in the image plane. The intensity profiles of spot diagrams constructed for M1 and M2 with nine sets of figure errors are shown in Fig. 13.

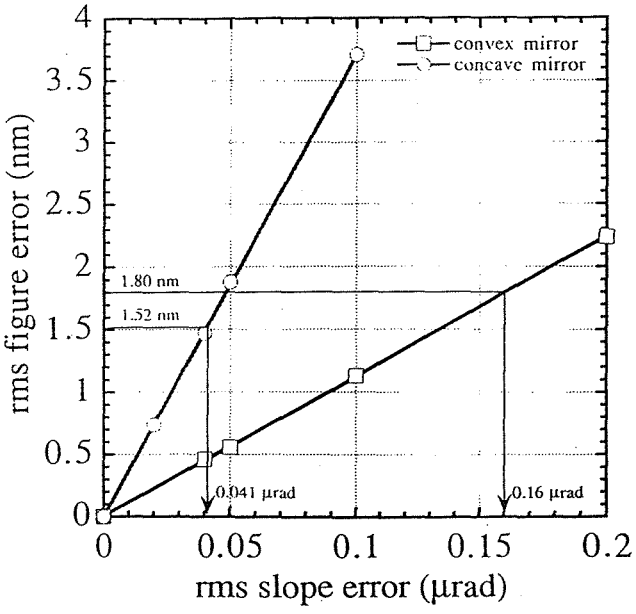

Fig. 12. Relation between the rms slope error and the rms figure error in the case of the NTT's projection system consisting of the ellipsoidal mirrors M1 and M2.

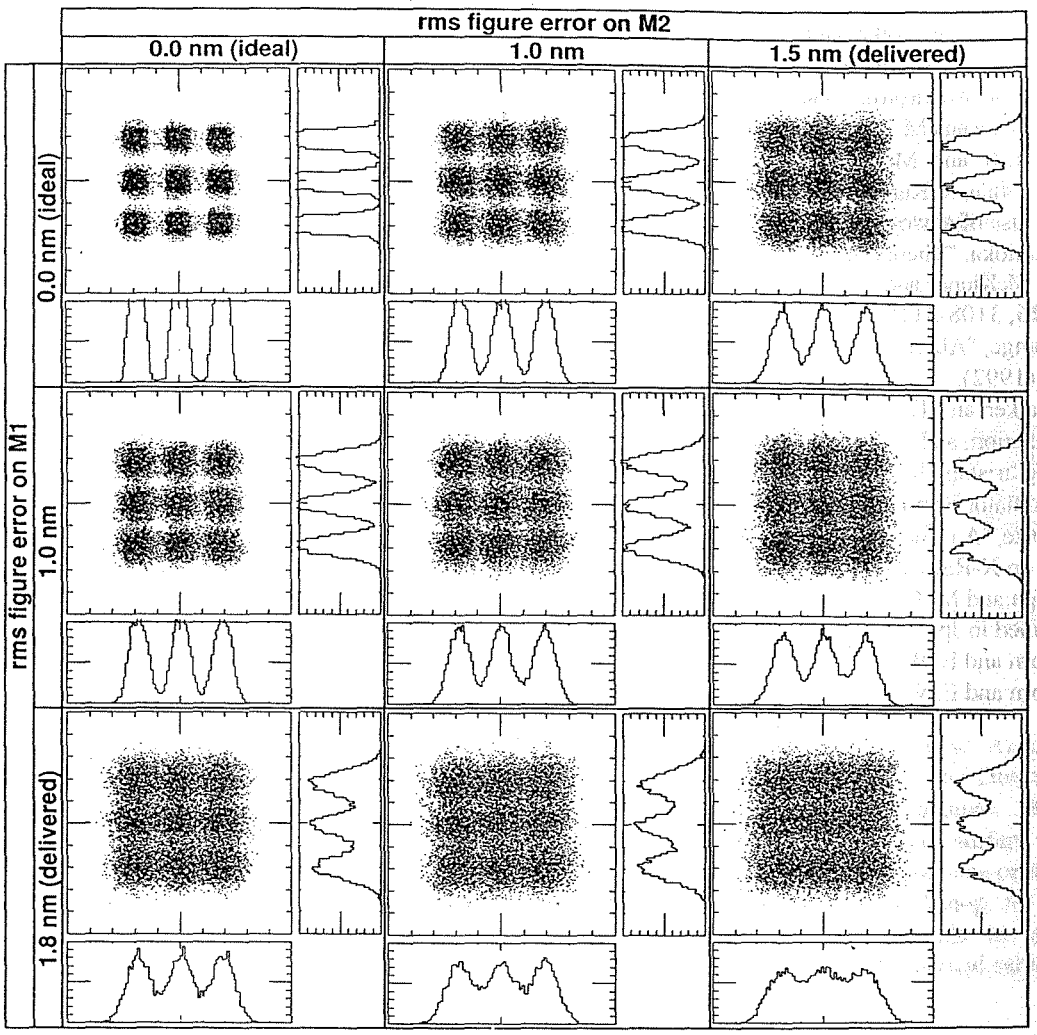

Fig. 13. Spot diagrams and their intensity profiles constructed for the demagnifying projection system with various sets of the rms figure errors of M1 and M2.

In Fig. 13 the rms figure errors are assumed to be σ_{FE} = 0, 1.0, and 1.8 nm for the convex ellipsoidal mirror M1 and σ_{FE} = 0, 1.0, and 1.5 for the concave ellipsoidal mirror M2. The "≥45%" criterion was applied to the modulations estimated from Fig. 13 and other similar spot diagrams. The result shows that any combination of σ_{FE}(M1) > 1.2 nm and σ_{FE}(M2) > 1.5 nm yields a modulation less than 45 %. We therefore adopt 1.2 nm and 1.5 nm as the tolerances for the rms figure errors of M1 and M2, respectively.

The surface figures of M1 and M2 fabricated were measured with a Zygo Mark IV interferometer. The rms (or Peak-to-Valley, P-V) values of the figure errors were found to be ~1.8 nm (or ~5.5 nm) and ~1.5 nm (or ~4.4 nm) for M1 and M2, respectively. The spot diagram and its intensity profiles constructed with these tolerance values are shown at the lower right of Fig. 13. The figure clearly shows that a 0.1-μm line-and-space pattern cannot be resolved with the projection optics fabricated, in agreement with the experimental result. This suggests the need for improved surface figures of M1 and M2. As stated above, the present simulation gave the tolerances of 1.2 nm (or 0.11 μrad) and 1.5 nm (or 0.04 μrad) for the rms figure error (or rms slope error) of M1 and M2, respectively. These values would ease the Maréshal condition of 0.46 nm rms for both M1 and M2, but their reliability still remains to be proved experimentally.

8. 2. Simulation of Foucault knife edge testing for assembly errors

This subject is reported by T. Haga and M. C. K. Tinone in the Proceedings of this workshop. The interested reader is referred to their article entitled "Numerical analysis of EUV optics assembly using at-wavelength Foucault testing" in this volume.

References

1. T. Namioka, M. Koike, and D. Content, "Geometric theory of the ellipsoidal grating," Appl. Opt. **33**, 7261-7274 (1994).
2. M. Koike and T. Namioka, "Optimization and evaluation of varied line spacing plane grating monochromators for third generation synchrotron radiation sources," J. Electron Spectrosc. Relat. Phenom. **80**, 303-308 (1996).
3. T. Namioka and M. Koike, "Analytical representation of spot diagrams and its application to the design of monochromators," Nucl. Instr. and Meth. A**319**, 219-227 (1992).
4. H. Kinoshita, K. Kurihara, T. Mizota, T. Haga, H. Takenaka, and Y. Torii, "Large-area, high-resolution pattern replication by the use of a two-aspherical-mirror system," Appl. Opt. **32**, 7079-7083 (1993).
5. T. Namioka, "Theory of the concave grating. I," J. Opt. Soc. Am. **49**, 446-460 (1959).
6. W. R. McKinney and C. Palmer, "Numerical design method for aberration-reduced concave grating spectrometers," Appl. Opt. **26**, 3108-3118 (1987).
7. R. Grange, "Aberration-reduced holographic spherical gratings for Rowland circle spectrographs," Appl. Opt. **31**, 3744-3749 (1992).
8. R. Walker and B. Diviacco, "URGENT – A computer program for calculating undulator radiation spectral, angular, polarization, and power density properties," Rev. Sci. Instrum. **63**, 392-395 (1992).
9. R. Beguiristain, M. Koike, and T. Namioka, "The effects of heat load on the performance of a grating monochromator on an undulator beamline: simulation," Proc. SPIE **2011**, 559-564 (1993).
10. M. Koike, "An efficient subroutine for simulating undulator radiation in ray tracing program," Book of Abstracts, 15th Int. Conf. on X-Rays and Inner-Shell Processes, Knoxville, 1990, paper B07.
11. T. Haga and M. C. K. Tinone, "Numerical analysis of EUV optics assembly using at-wavelength Foucault testing," to be published in Jpn. J. Appl. Phys.
12. M. Born and E. Wolf, *Principles of Optics*, 5th ed., (Pergamon Press, New York, 1975), p. 468.
13. M. Born and E. Wolf, *Principles of Optics*, 5th ed., (Pergamon Press, New York, 1975), p. 469.